G4-binding drugs, chlorpromazine and prochlorperazine, repurposed against COVID-19 infection in hamsters

Shuvra Shekhar Roy[1,2], Shalu Sharma[1,2], Zaigham Abbas Rizvi[3], Dipanjali Sinha[1,2], Divya Gupta[4], Mercy Rophina[1,2], Paras Sehgal[1,2], Srikanth Sadhu[3], Manas Ranjan Tripathy[3], Sweety Samal[5], Souvik Maiti[1,2,6], Vinod Scaria[1,2], Sridhar Sivasubbu[1,2], Amit Awasthi[3], Krishnan H. Harshan[2,4], Sanjeev Jain[7] and Shantanu Chowdhury[1,2]*

[1]CSIR-Institute of Genomics & Integrative Biology, New Delhi, 110025, India, [2]Academy of Scientific & Innovative Research (AcSIR), Ghaziabad, 201002, India, [3]Immuno-biology Laboratory, Infection and Immunology Centre, Translational Health Science and Technology Institute, Faridabad, 121001, India, [4]CSIR-Centre for Cellular and Molecular Biology, Hyderabad, 500007, India, [5]Translational Health Science and Technology Institute, Faridabad, 411008, India, [6]CSIR-National Chemical Laboratory, Pune, 121001, India, [7]Molecular Genetics Laboratory, National Institute of Mental Health and Neurosciences (NIMHANS), Bengaluru, 560029, India

The COVID-19 pandemic caused by SARS-CoV-2 has caused millions of infections and deaths worldwide. Limited treatment options and the threat from emerging variants underline the need for novel and widely accessible therapeutics. G-quadruplexes (G4s) are nucleic acid secondary structures known to affect many cellular processes including viral replication and transcription. We identified heretofore not reported G4s with remarkably low mutation frequency across >5 million SARS-CoV-2 genomes. The G4 structure was targeted using FDA-approved drugs that can bind G4s - Chlorpromazine (CPZ) and Prochlorperazine (PCZ). We found significant inhibition in lung pathology and lung viral load of SARS-CoV-2 challenged hamsters when treated with CPZ or PCZ that was comparable to the widely used antiviral drug Remdesivir. In support, *in vitro* G4 binding, inhibition of reverse transcription from RNA isolated from COVID-infected humans, and attenuated viral replication and infectivity in Vero cell cultures were clear in case of both CPZ and PCZ. Apart from the wide accessibility of CPZ/PCZ, targeting relatively invariant nucleic acid structures poses an attractive strategy against viruses like SARS-CoV-2, which spread fast and accumulate mutations quickly.

1 Introduction

Since the emergence of SARS-CoV-2 more than 500 million infections and more than 6 million deaths have been confirmed (https://covid19.who.int/, as of 31st May 2022). Recommended treatments for COVID-19 include immunomodulatory molecules like JAK inhibitors, IL-6 receptor blockers, systemic corticosteroids; monoclonal antibodies targeting the spike protein of SARS-CoV-2; and drugs like Remdesivir and Molnupiravir that target viral replication (WHO; Janik et al., 2021; Kelleni, 2021). However, these are not readily accessible in a global context underlining a critical need for developing both effective and affordable therapeutic strategies against SARS-CoV-2.

Sequences within viral genomes adopt secondary structures that can be targeted using ligands as potential antiviral drugs (Ruggiero and Richter, 2018; 2020; Abiri et al., 2021; Ruggiero et al., 2021). DNA or RNA sequence motifs with four or more runs of guanine repeats interspersed with short runs of other bases form non-canonical secondary structures called G-quadruplexes (G4s) (reviewed in Mukherjee et al., 2019; Sengupta et al., 2020; Varshney et al., 2020). Further, G4s were shown to be predominant in gene regulatory regions across organisms through specific G4-binding transcription factors (Rawal et al., 2006; Verma et al., 2008; Yadav et al., 2008; Thakur et al., 2009; Dhapola and Chowdhury, 2016); and, RNA G4s within mRNA were shown to inhibit translation by stalling or dissociation of ribosomes (Arora et al., 2008; Murat et al., 2014; Kharel et al., 2020; Lyu et al., 2021). Notably, recent studies identified potential G4s (pG4) in the SARS-Cov2 genome (Supplementary Figure S1) (Zhang et al., 2020; Bezzi et al., 2021; Ji et al., 2021; Ruggiero et al., 2021). These identified pG4 sequences were observed to be able to form G4 structures and interact with both viral and human proteins (Bezzi et al., 2021; Ji et al., 2021; Ruggiero et al., 2021). This indicates the importance of these secondary viral RNA structures in the biology of the virus and poses them as viable drug targets. Interestingly, all these pG4s identified so far only have 2 G-quartets.

To target SARS-CoV-2 we sought to test FDA-approved drugs reported to bind to G4s (Mergny and Helene, 1998; Castillo-Gonzalez et al., 2013). Here we show two such drugs chlorpromazine (CPZ) and prochlorperazine (PCZ) (Castillo-Gonzalez et al., 2013) decrease infectivity, viral load, and pathology of SARS-CoV-2 infection in the hamster model. This was further supported with intracellular results using the Vero cell infection model. Both CPZ and PCZ bound to a novel SARS-CoV-2 RNA G4 and inhibited reverse transcription suggesting attenuated viral replication and transcription within the Vero cells in presence of CPZ/PCZ. Together these support the function of CPZ and PCZ as molecules with anti-COVID-19 activity with potential for repurposing as affordable drugs against SARS-CoV-2.

2 Results

2.1 G4 motifs in the SARS-CoV-2 genome remarkably resistant to mutations

The SARS-CoV-2 genome sequence was examined for potential G4-forming (pG4) sequence. We identified two pG4s having three

G-quartets within the ORF1a/ORF1ab gene (pG4-1 and pG4-2; Table 1) not reported earlier. The pG4s included breaks within the G-stretches thus allowing bulge formations for stable G4 structure formation as deduced from multiple published G4-stability scoring algorithms (Supplementary Table S1) (Beaudoin et al., 2014; Bedrat et al., 2016; Garant et al., 2017; Hon et al., 2017; Garant et al., 2018). In an earlier genome-wide study in humans we noted pG4s to be relatively impervious to mutations compared to other regions of the genome, supporting physiological relevance of pG4s (Baral et al., 2012). Here we reasoned, if functionally significant the newly identified pG4s might be relatively less prone to mutations. Importantly, if so, such pG4s could be crucial for any approach that targets different variants of SARS-CoV-2.

Reported mutations within more than 5 million SARS-CoV-2 genomes (5406687 genome sequences retrieved from China National Center for Bioinformation- National Genomics Data Center as of 28th of May 2022) was analysed: On average each nucleotide was mutated ~158 times per 100000 sequenced genomes (frequency: 0.00158; Figure 1A). The average mutation frequency of the Gs within the newly identified pG4s was significantly lower: ~22 and 44 per 100000 SARS-CoV-2 genomes (frequency: 0.00022 and 0.00044) for pG4-1 and pG4-2, respectively (Figures 1B, C).

We also checked the mutation frequency of another previously well characterised pG4 with two G-tetrads designated as RG-1 by authors (Zhao et al., 2021). The Gs in RG-1 pG4 had a relatively high mutation frequency of 0.0311 as a constituent G was highly mutated across samples (Figure 1C). Based on these we further focused on pG4-1, which appeared to be most conserved among the studied G4s, for further experiments.

2.2 ORF1 pG4-1 forms a G4 structure

Circular Dichroism (CD) spectrum of the RNA sequence representing pG4-1 showed positive/negative peaks at 260/240 nm respectively confirming the formation of a G4 structure with parallel topology (Figure 2A) (del Villar-Guerra et al., 2018). In contrast, for a similar RNA sequence where specific Gs were substituted (mutated-control RNA), the positive/negative CD peaks were significantly attenuated supporting specificity of the folded RNA G4 (Figure 2A).

Formation and stability of the G4 was also tested using N-methyl mesoporphyrin IX (NMM), a G4 binding ligand that gives enhanced fluorescence upon binding specifically to G4s (Kreig et al., 2015). The fluorescence of NMM was enhanced by more than hundred-fold in presence of the pG4-1, but not in case of the mutated-control RNA sequence (Figure 2B). Together these support RNA G4 formation by the pG4-1 RNA sequence.

2.3 CPZ and PCZ bind to ORF1 pG4-1

To design a small-molecule induced targeting we next asked if pG4-1 binds to the G4 binding ligands CPZ and/or PCZ, which are FDA approved drugs (DRANSFIELD, 1958; Castillo-Gonzalez et al., 2013). CPZ and PCZ were chosen as they had the highest

TABLE 1 New pG4s identified in the SARS-CoV-2 genome that have bulges. Their sequences, genomic positions are mentioned.

PQS	Sequence	Genomic position
pG4-1	GGGUAUUAAAAUACAAGAGGGUGUGGUUGAUUAUGG	NC_045512v2:4,486-4,521
pG4-2	GGGUCAGGGUUUAAAUGGUUACACUGUAGAGG	NC_045512v2:4,255-4,286

FIGURE 1
pG4 motifs in the SARS-CoV-2 genome are conserved. **(A)** Mutation frequency (number of sequenced genomes with mutation at a given base position/total number of sequenced genomes) of each nucleotide of the SARS-CoV-2 genome plotted against their respective genomic positions. The average mutation frequency is marked in yellow. Location of RG-1 has been denoted. The circos plot was prepared using ggplot2 package in R.**(B)** Mutation frequency within the 4,000-5,000 bp positions to clearly denote the mutation frequency of pG4-1 and pG4-2. The line histogram was prepared using GraphPad Prism. **(C)** The sequences of pG4-1, pG4-2 and RG-1 with the Gs used to calculate the average mutation frequency marked in bold. In RG-1, one of the Gs has a very high mutation frequency for a G to T mutation (marked in red). The genome-wide mutation counts and mutation frequency analysis raw data are submitted as a supporting information file.

G4-stabilising effects among the G4-stabilizing drugs tested in Castillo-Gonzalez et al., 2013. Isothermal titration calorimetry (ITC) showed both CPZ and PCZ interact with pG4-1 with dissociation constants in the micromolar range: The binding between CPZ and pG4-1 was monophasic (K_d = 39.0 ± 1.78 μM), whereas PCZ binds to pG4-1 in a biphasic manner

FIGURE 2
pG4-1 can form a G4 structure. **(A)** CD spectra of 5 µM of pG4-1 WT and its mutated control, pG4-1 Mut where specific 'G's were mutated to 'A's to prevent G4 formation. **(B)** Fluorescence spectra of 1 µM NMM only or in presence of 1 µM pG4-1 WT or pG4-1 Mut.
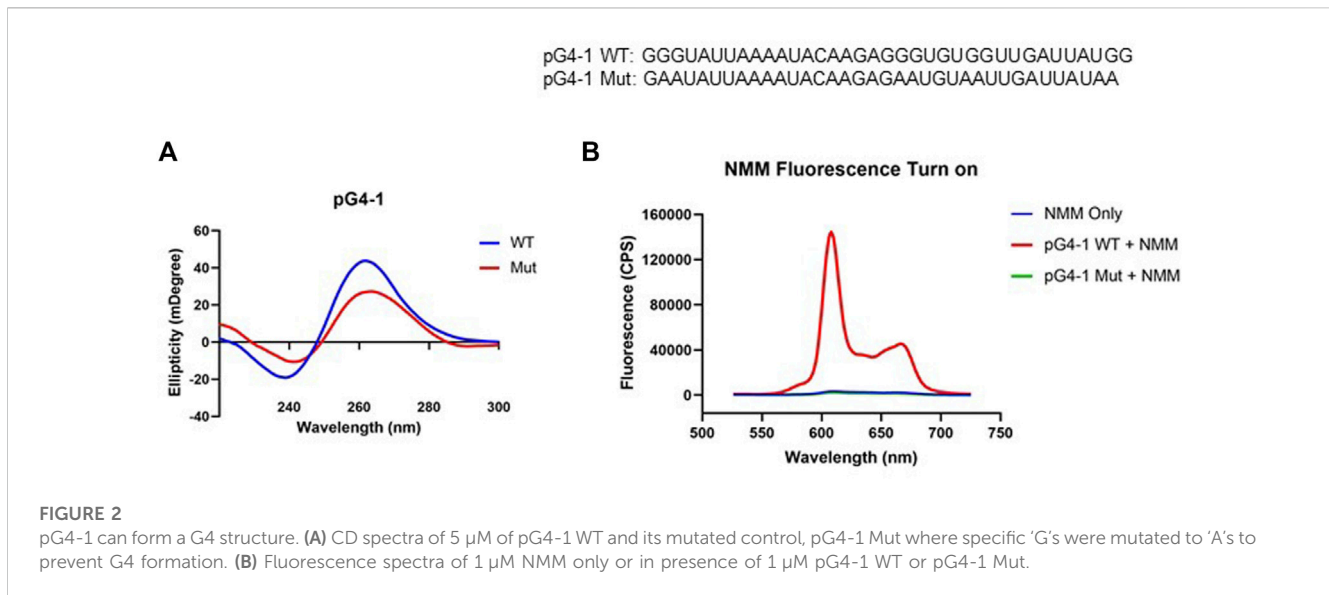
($K_{d1} = 32.1 \pm 5.56$ µM, $K_{d2} = 39.0 \pm 1.78$ µM) (Figures 3A, B). CD of pG4-1 was performed in presence of increasing concentrations of the ligands CPZ and PCZ to test whether interaction with the ligands affected the topology of pG4-1. Results showed reduced amplitude of the positive/negative CD peaks without any change in the position of the CD peak confirming interaction of pG4-1 with CPZ and PCZ retained the parallel topology (Figures 3C, D).

We reasoned that specific binding of CPZ and PCZ with pG4-1 would compete with G4-bound-NMM resulting in reduced fluorescence from G4-NMM interaction (see above). Increasing concentration of CPZ and PCZ resulted in reduction of fluorescence from G4-NMM with more than fifty percent decrease at a molar ratio of 1:40. Together these supported specific association of both CPZ and PCZ with the RNA G4 formed by ORF1 pG4-1 (Figures 3E, F).

2.4 G4 bound CPZ and PCZ can inhibit reverse transcriptase processivity

Ligand binding of RNA G4s can inhibit mammalian translation as well as replication and transcription of some viruses, *via* stalling and/or dissociation of polymerases or ribosomes (Murat et al., 2014; Butovskaya et al., 2019; Kharel et al., 2020; Lyu et al., 2021; Majee et al., 2021; Lv et al., 2022). Here we tested whether binding of CPZ/PCZ to RNA G4 affected reverse transcription. For this a synthetic SARS-CoV-2 genomic RNA template was obtained where the whole viral genome was represented by six non-overlapping 5 kb fragments. This template was reverse transcribed using specific primers such that ORF1 pG4-1 or a non-G4 forming control region was reverse transcribed. Following this, specific primers encompassing the pG4-1 or the selected control region were used for quantitative RT-PCR to assay the levels of reverse transcription (see Methods). Reverse transcription of the pG4-1 harbouring region was significantly reduced in presence of both CPZ and PCZ relative to untreated samples. This was observed after normalizing the effects of CPZ and PCZ on the reverse

transcription of the control region (Figure 4A). Together these showed reduced reverse transcription from the pG4-1-harbouring region due to inhibition of reverse transcriptase processivity by G4 bound CPZ or PCZ.

To test in human patient samples, we used RNA isolated from nasopharyngeal swabs of five COVID-19 infected individuals. Due to the paucity of patient sample RNA only CPZ was tested. Notably, inhibition of reverse transcription in all the five samples was clear in presence of 5 µM CPZ (Figure 4B) suggesting interaction of CPZ with pG4-1 restricts processivity of the reverse transcriptase. Though reverse transcriptases are not present in SARS-CoV-2, these experiments suggest the G4 bound drugs might affect other translocating complexes/enzymes like RNA dependent RNA polymerase (*RdRp*). However, it must be noted that the extent and mechanism of inhibition of *RdRp* by these drugs has not been studied.

2.5 CPZ and PCZ can inhibit SARS-CoV-2 infectivity in vero cells

Next, we sought to test whether CPZ and PCZ affect the infectivity of SARS-CoV-2 and viral replication within cells. Vero cells were infected with SARS-CoV-2 virus at 1 MOI for 3 h at 37°C in the presence of the respective inhibitors CPZ or PCZ either at 2 µM or 5 µM. After the inoculum was removed and the cells were washed, treatment was continued in 10% FBS medium for another 24 h. At 24 hpi the media was replaced by fresh media containing the respective inhibitors. At 48 hpi supernatants were collected for plaque formation assay and viral RNA quantification.

Treatment with 5 µM of CPZ or PCZ led to significant decrease in plaque formation, 25% and 60% for CPZ and PCZ respectively, and therefore infectivity of the virus (Figure 4C; Supplementary Figure S2). The levels of viral RNA genes are indicative of viral replication and reproduction after infection. Real-time PCR quantification of the *RdRp* (RNA-dependent RNA
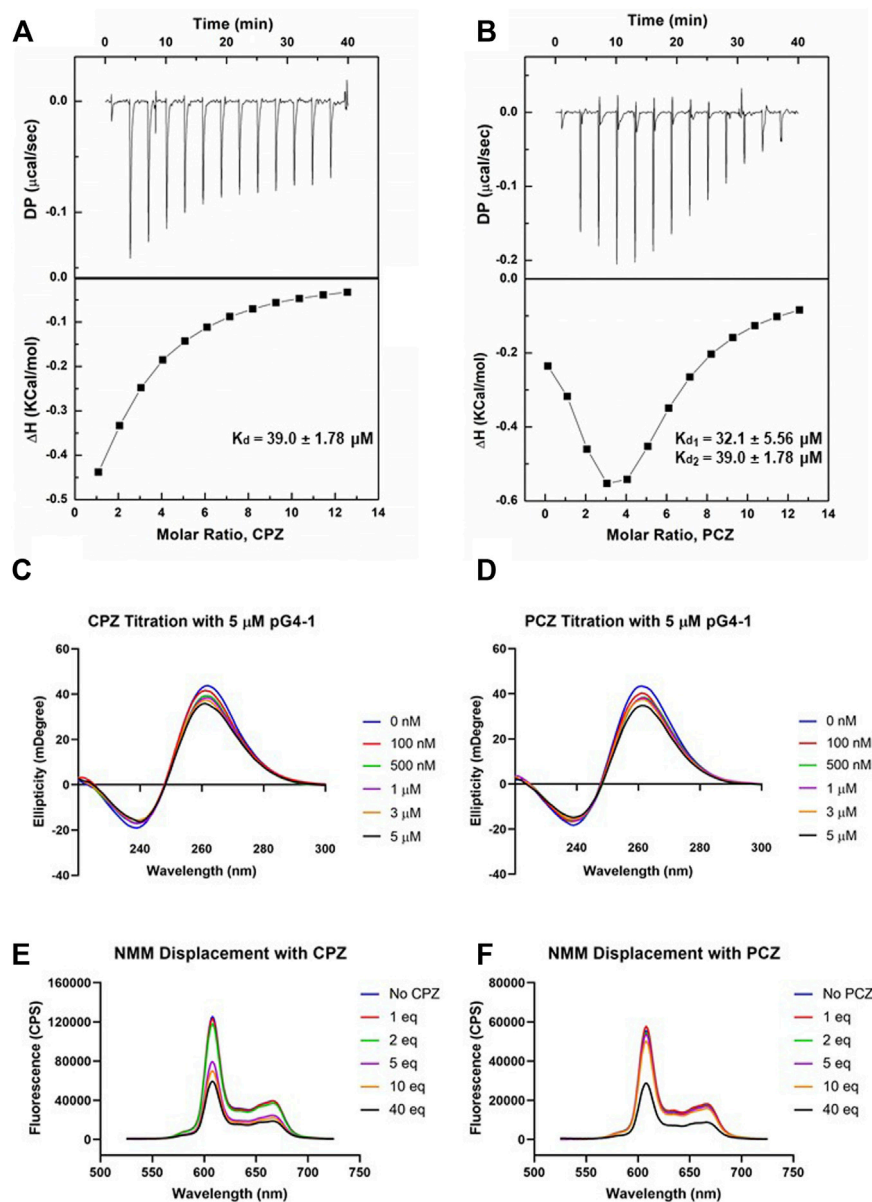
FIGURE 3
FDA approved drugs CPZ and PCZ can bind to pG4-1. Isothermal titration calorimetry (ITC) profiles for the titration of CPZ **(A)** or PCZ **(B)** with ORF1 pG4-1. The upper panels show sequential injection of the ligands into ORF1 pG4-1; fitted data of integrated heat values after correction for heat of dilution plotted against molar ratio shown in lower panels; dissociation constants mentioned in the lower panel. CD spectra of ORF1 pG4-1 with increasing concentration of CPZ **(C)** or PCZ **(D)**. Fluorescence spectra of 1 μM of NMM in presence of 1 μM of ORF1 pG4-1 with increasing molar ratio of CPZ **(E)** or PCZ **(F)**.

polymerase), *E* (envelope), *N* (Nucleocapsid) and *ORF1* genes were done using RNA isolated from the collected supernatants. At 5 μM, both CPZ and PCZ treatment reduced expression of *RdRp, E, N* and *ORF1* by more than 60% (Figure 4D). However, we noted 5 μM PCZ inhibited growth of Vero cells (MTT assay, Supplementary Figure S3A), whereas treatment with a lower concentration of 2 μM PCZ did not result in cytotoxicity while still reducing expression of the viral *RdRp* and *E* genes (Supplementary Figures S3B, 4). Though there was marginal cytotoxicity in 5 μM CPZ treatment as well, the impact on the viral RNA appears to be more significant.

2.6 CPZ and PCZ treatment alleviates COVID-19 pathogenesis in hamsters

To check the effect of the G4 binding ligands as potential molecules for therapeutic intervention in COVID-19 treatment we used SARS-CoV-2 infection in hamsters as previously described (Chan et al., 2020; Sia et al., 2020; Rizvi et al., 2021; 2022b). Both prophylactic and therapeutic regimens of CPZ and PCZ treatment were tested. Prophylactic groups of hamsters received 8 mg/kg or 5 mg/kg of CPZ and PCZ (mentioned as pCPZ and pPCZ to denote prophylactic arm of the experiment)
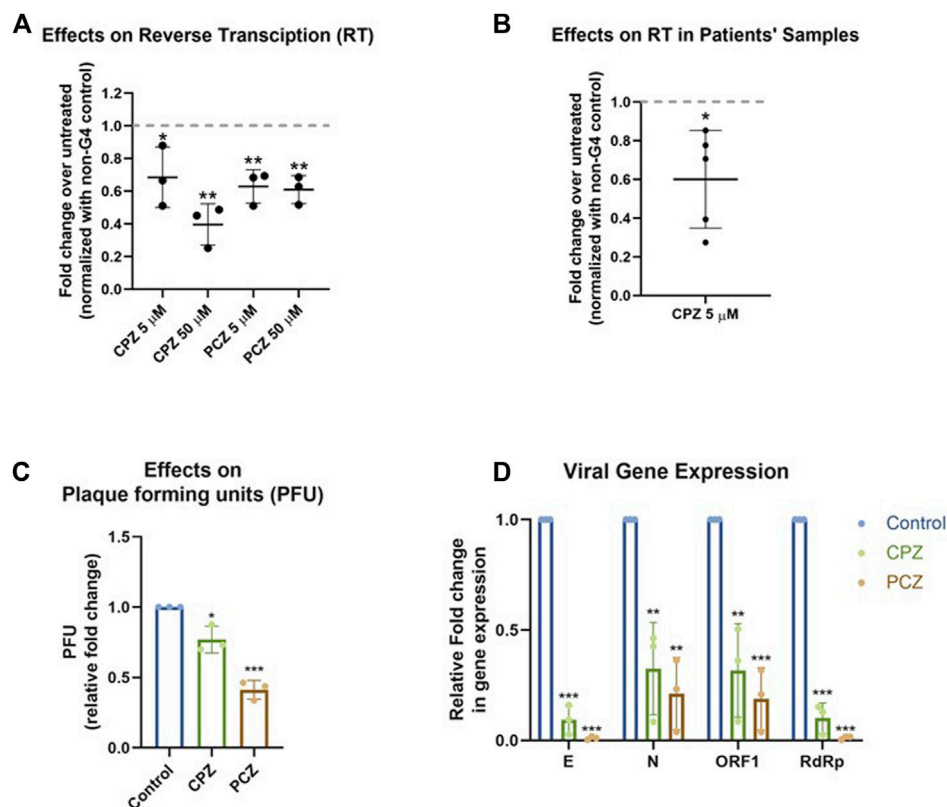
FIGURE 4
CPZ, PCZ inhibit viral replication in cells *via* G4 binding. **(A)** Fold change in reverse transcription of the ORF1 pG4-1 harbouring region over untreated control using a synthetic SARS-CoV-2 RNA: different concentrations of CPZ and PCZ were used; a non-G4 forming region was used for normalization. Mean $\pm$ SD (n = 3); unpaired, two-tailed t-test. **(B)** Fold change in reverse transcription of the ORF1 pG4-1 harbouring region over untreated control in RNA isolated from nasopharyngeal swabs of COVID-19 infected individuals, treated with 5 μM CPZ; a non-G4 forming region was used for normalization. Mean $\pm$ SD (n = 3); unpaired, two-tailed t-test. **(C)** Fold change in plaque formation units (PFUs) indicating infectivity of supernatant from infected Vero cells treated with 5 μM of CPZ or PCZ compared against untreated control. Mean $\pm$ SD (n = 3); unpaired, two-tailed t-test. **(D)** Expression of the RNA levels of E, N, ORF1 and RdRp genes of SARS-CoV-2 in the extracellular media of infected Vero cells treated with 5 μM of CPZ or PCZ compared against untreated control. Mean $\pm$ SD (n = 3); unpaired, two-tailed t-test.

respectively through intraperitoneal administration each day starting from 3 days prior to the SARS-CoV-2 challenge till the end point (day 4 post infection). In the therapeutic group CPZ and PCZ (tCPZ and tPCZ to denote therapeutic arm), the hamsters received the drug 8 mg/kg and 5 mg/kg respectively through intraperitoneal injection every day from the day of challenge till the end point (Diaconu et al., 2010; Simanjuntak et al., 2015). FDA approved drug Remdesivir, which has been shown to work as a potent antiviral against SARS-CoV-2 infection, was used as a control with 15 mg/kg subcutaneous injections given 1 day before and after the challenge (Beigel et al., 2020; Pruijssers et al., 2020; Rizvi et al., 2022b).

From day 2 onwards, we noted the treatment groups had protection against body weight loss compared to the infected control group (Figure 5A). Hamsters receiving prophylactic treatment of CPZ showed no body weight loss and the trend in percent body weight change was comparable to the Remdesivir control group. Notably, prophylactic treatment of CPZ showed improved rescue of body weight loss than the prophylactic PCZ group, as well as their respective therapeutic groups, suggesting CPZ pre-treatment might be more effective in rescuing body weight loss in SARS-CoV-2 challenged hamsters (Figures 5A, B).

All the animals were euthanized on day 4 following challenge, which has been shown earlier as the optimal time point to study SARS-CoV-2 lung pathology in hamsters (Rizvi et al., 2021, 2022b). Regions of pneumonia observed in the lungs of the infected animals were significantly reduced in drug-treated group in a manner similar to the remdesivir control group (Figure 5C). In order to further understand the anti-viral efficacy of the G4 binding drugs, qPCR for the N gene was performed using RNA isolated from the lung samples of the hamsters for relative estimation of lung viral load (Figure 5D). This showed significant decrease in expression of the N gene in both PCZ and CPZ groups. Notably, when compared to the Remdesivir control group, PCZ as well as CPZ administration showed similar or more decrease in viral load than Remdesivir treatment both in prophylactic and therapeutic regime validating the potent anti-viral nature of these drugs. Interestingly, drop in the expression of the N gene was not fully in line with the body weight changes in the treatment groups; however, the prophylactic groups showed marginal gain in body weight in both CPZ and PCZ at later stages of infection.

To further understand the mitigation in SARS-CoV-2-mediated lung pathology in CPZ/PCZ treated groups we carried out lung histopathological analysis through hematoxylin and eosin (H and
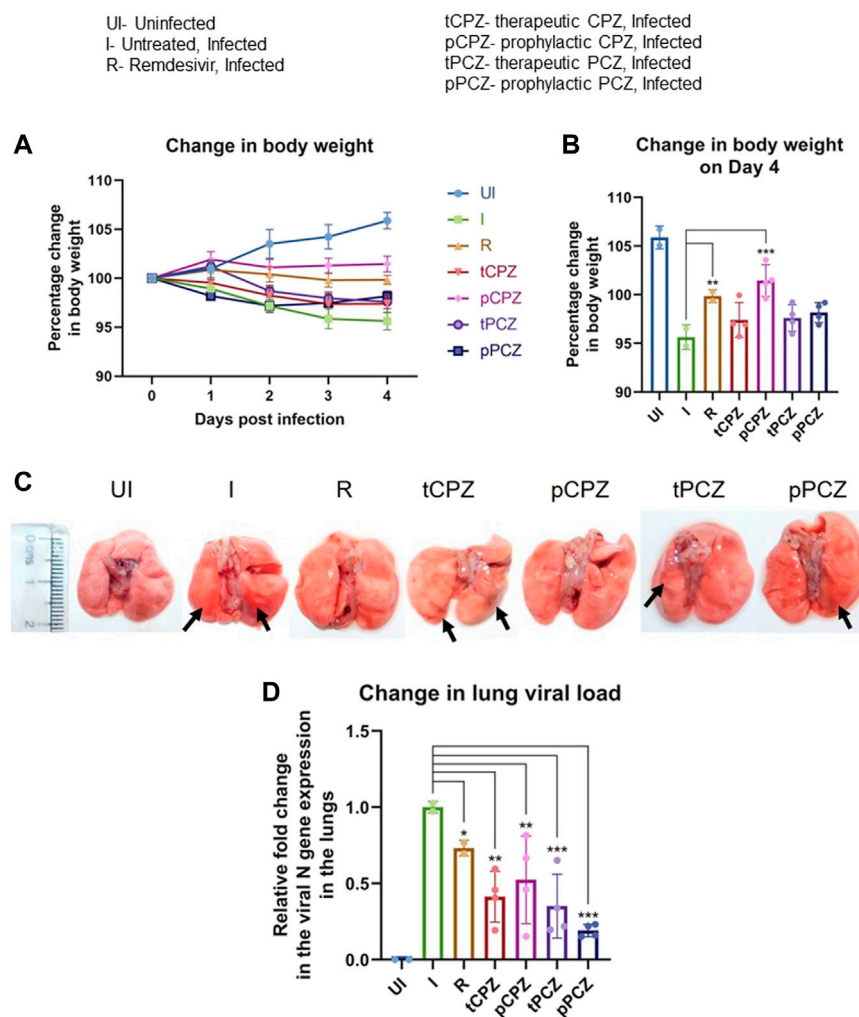
FIGURE 5
CPZ, PCZ inhibits viral infection in the hamster lungs. **(A)** Percentage (%) change in body weight of hamsters of different treatment groups: uninfected (UI), infected (I), infected with Remdesivir treatment (R), infected with prophylactic treatment of CPZ (pCPZ) and PCZ (pPCZ), infected with therapeutic treatment of CPZ (tCPZ) and PCZ (tPCZ). **(B)** Percentage % change in body weight of hamsters of different treatment groups on the fourth day post infection. Mean $\pm$ SE (n = 3); ordinary one-way ANOVA. **(C)** Images of the excised lungs from hamsters of different treatment groups, showing gross morphology with pneumonitis region. **(D)** Relative fold change in the N gene expression of SARS-CoV-2 representing viral load in the lung samples of the hamsters of different treatment groups. Mean $\pm$ SE (n = 3); ordinary one-way ANOVA.

E)–staining. The treated groups showed reduction in pneumonitis, bronchitis and inflammation similar to that of the Remdesivir control group (Figures 6A, B). In addition, we noted that the difference in alveolar epithelial injury was not significantly different in any of the drug treated groups compared to infected untreated control. Considering the overall disease score, both CPZ and PCZ could significantly reduce the lung pathology arising from the infection in a manner similar to the Remdesivir control group. Furthermore, size and mass of the spleen of the animals were compared to evaluate gross morphological changes as splenomegaly can be a critical indicator of active infection (Rizvi et al., 2021, 2022b). Importantly, the CPZ/PCZ treated groups showed reduced splenomegaly similar to Remdesivir treatment (Figures 6C, D).

3 Discussion

While focusing on canonical G4s to target in the SARS-CoV-2 genome we first noted that the pG4s identified so far harboured two G-tetrads (i.e., with repeats constituting 2Gs that form 2 guanine-tetrads). Typically, these tend to be less stable than G4s made of three G-tetrads (Kikin et al., 2006; Hon et al., 2017). Here we identified two new pG4s with three G-tetrads that included bulges—a form of G4 that has been widely studied and understood to be stable in solution (Sengupta et al., 2020; Varshney et al., 2020). On genome wide mutation frequency analysis using more than five million reported SARS-CoV-2 genomes we found, surprisingly, that the G4s were also significantly resistant to mutations. Selecting the more conserved of the two G4s we showed that it can form a
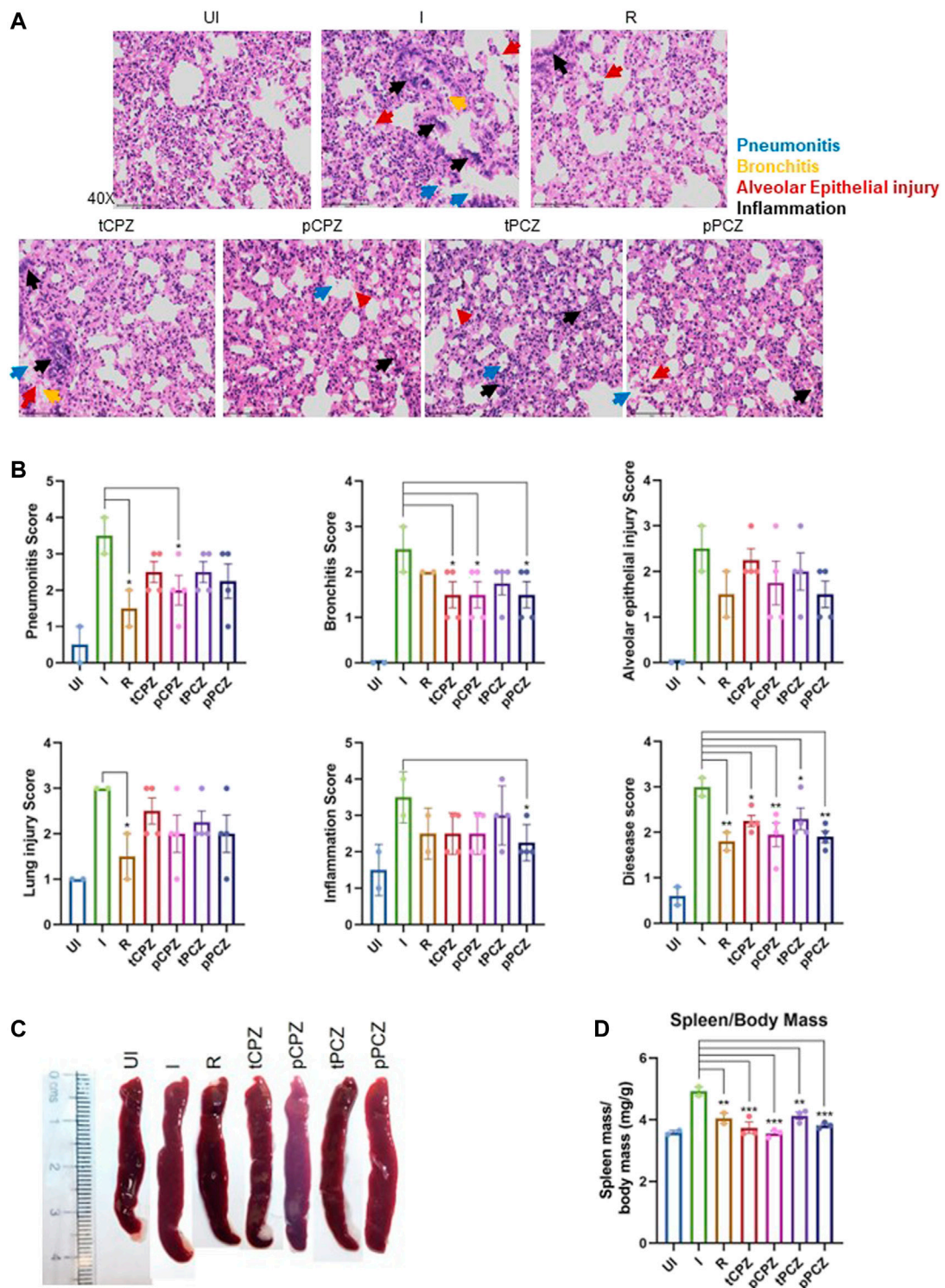
FIGURE 6
Histopathology shows better prognosis in SARS-CoV-2 infected hamsters upon CPZ, PCZ treatment. **(A)** Images of H&E-staining of excised lungs from hamsters of different treatment groups at ×40 magnification showing regions of pneumonitis (blue arrow), bronchitis (orange arrow), alveolar epithelial injury (red arrow), and inflammation (black arrow). **(B)** Histological score for pneumonitis, bronchitis, alveolar epithelial injury, lung injury, inflammation, and overall disease score of the lungs after different treatments. **(C)** Representative images of excised spleen indicating changes in the spleen length upon different treatments. **(D)** Spleen mass/body mass (mg/g) of the excised spleen indicating splenomegaly upon different treatments. Mean $\pm$ SE (n = 3); ordinary one-way ANOVA.

stable G4 structure. We selected the more conserved G4 as mutations within the G4 would effectively rule out the target in mutant strains. CPZ and PCZ, two FDA approved drugs, bind to the G4 with micromolar affinity, and inhibited reverse transcription from synthetic as well as RNA isolated from patients suggesting potential anti-COVID activity. While the *in vitro* studies focused on G4-1, we cannot rule out binding of CPZ/PCZ to other G4s. In Vero cells CPZ and PCZ inhibited SARS-CoV-2 infection and also decreased viral replication and transcription. Prompted by these results we asked whether CPZ and/or PCZ could affect infection in the hamster animal model: Notably, CPZ and PCZ decreased disease pathogenesis in terms of body weight loss, lung viral load, lung histopathology and splenomegaly. The effects of CPZ and PCZ were remarkably comparable to that of treatment with the standard-of-care antiviral Remdesivir. Though there was some cytotoxicity from drug treatment in the Vero cells the drugs also lowered viral titers in the hamster model without any significant toxicity (as indicated by the increase in body weight in the drug treated animals over the control infected animals (Figures 5A, B). This led us to conclude that the antiviral effects override the cytotoxic effects of the drugs.

Golden Syrian hamsters have been previously described as a suitable model for SARS-CoV-2 infection which mimics viral entry and replication which is similar to that of humans. It has been shown that SARS-CoV-2 infection in hamsters leads to pathological manifestations as seen in clinical cases such as lung pneumonitis, inflammation, and alveolar epithelial injury (Boudewijns et al., 2020; Chan et al., 2020; Lee et al., 2020; Sia et al., 2020). Hamsters have been conventionally used as a model for most of the anti-viral therapeutic drugs and vaccine studies (Kreye et al., 2020; Rosenke et al., 2020; Tostanoski et al., 2020; Rizvi et al., 2022a). Hence, we used young adult hamsters for our study which represents majority of the SARS-CoV-2 infected population.

Earlier studies suggested the significance of RNA G4s in infectious human viruses, and a few recent reports focused particularly on G4s in SARS-CoV-2 (Zhang et al., 2020; Bezzi et al., 2021; Ji et al., 2021; Ruggiero et al., 2021). Nsp13, a viral helicase almost identical on SARS-CoV and SARS-CoV-2, was reported to bind SARS-CoV-2 G4s (Ji et al., 2021). Nsp3, another coronavirus protein, was shown to bind human host cell RNA G4s through the SARS-Unique Domain (SUD) of Nsp3 (Lavigne et al., 2021). Further work showed CNBP - a human cell protein that is elevated on infection and binds to SARS-CoV-2 genome - binds and unfold G4s from the SARS-CoV-2 genome *in vitro* (David et al., 2019; Bezzi et al., 2021; Ruggiero et al., 2021; Schmidt et al., 2021). In addition, RG-1 region in the N gene of the SARS-CoV-2 was found to form a G4 structure that could be targeted using a G4 binding ligand (Zhao et al., 2021). On the other hand, stabilization of a G4 within the mRNA of human TMPRSS2, which was elevated in the lungs of COVID-19 patients, inhibited TMPRSS2 translation leading to prevention of SARS-CoV-2 entry (Liu et al., 2022). Together these suggest the significance of RNA G4s, both viral and host, in the replication, transcription, and assembly of SARS-CoV-2 (Panera et al., 2020; Ruggiero et al., 2021).

CPZ and PCZ was implicated to be able to abrogate host cell infection by hepatitis C, dengue and some coronaviruses by inhibiting clathrin-mediated endocytosis (Chamoun-Emanuelli et al., 2013; Burkard et al., 2014; Simanjuntak et al., 2015; Cong et al., 2018; Stip et al., 2020). Intracellular calcium in host cells is necessary for viral entry and viral replication enabling infection of host cells (Chen et al., 2019; Jayaseelan and Paramasivam, 2020). Studies on SARS-CoV and MERS-CoV have observed that these viruses require calcium ions for membrane fusion and entry, with increase in intracellular calcium enhancing fusion of MERS-CoV (Lai et al., 2017; Straus et al., 2020). CPZ was reported to be able to inhibit store-operated calcium entry in cells (Choi et al., 2001). It must also be noted that CPZ and PCZ are used as antipsychotic and antidepressant drugs based on their effect on dopamine D2 and alpha-2 adrenergic receptors (Dransfield, 1958). A recent study further suggested antipsychotic drugs might be inhibiting viral replication (Fred et al., 2022). Another recent study observed inhibition of the replication of SARS-CoV-2 in cell lines by CPZ, however the mechanism behind this inhibition was not investigated (Plaze et al., 2021). A clinical trial found that second-generation antipsychotics was associated with decreased risk of COVID-19 infection in patients in the New York State–wide psychiatric hospital system (Nemani et al., 2022). Interestingly, though the decrease in risk of infection with CPZ (a first-generation antipsychotic) was not quite statistically significant, none of the 47 COVID-19 infected patients taking CPZ died of COVID-19 related causes. Along with the better inhibitory effects observed in the prophylactic treatment in hamsters this indicates the possibility of the role of CPZ/PCZ in inhibiting SARS-CoV-2 viral entry as well. It is therefore likely that the effect of CPZ/PCZ against SARS-CoV-2 infection is not solely due to their G4 binding ability but through multiple mechanisms that affect both the host and the virus. The prophylactic and therapeutic activity of CPZ/PCZ observed by us against COVID-19 infection in hamsters (Figures 5, 6) support this.

In conclusion, this is the first report showing FDA approved drugs CPZ and PCZ as potentially useful treatment options for COVID-19 due to its wide availability and relative affordability. We focused on targeting RNA structure in the form of G4s in the viral genome. Results demonstrate that secondary nucleic acid structures, that are relatively invariant (with low mutation frequency) in pathogenic genomes, could be effective targets against fast mutating strains like SARS-CoV-2.

4 Materials and methods

4.1 Reagents

Chlorpromazine and Prochlorperazine were purchased in the form of hydrochloride and dimaleate salt respectively, from Sigma (USA). The source of Remdesivir was Hetero Labs Limited received as a kind gift from Dr. Anil Kumar Pandey (ESIC Hospital, Faridabad). All the RNA oligos were purchased from Sigma of HPLC-purified grade. The sequences of the oligonucleotides used in these studies are presented in Table-1. Concentration of oligonucleotides solution were determined from absorbance at 260 nm using molar extinction coefficient at 260 nm of 384.2 and 401.5 M^{-1} cm^{-1} for ORF1 WT and ORF1 Mut sequences respectively. Nuclease free water (DEPC untreated) was used throughout all the

experiments. All biophysical experiments were done in 10 mM sodium cacodylate buffer (pH 7.4) containing 100 mM KCl at 25°C unless mentioned otherwise. The RNA oligos were heated at 95°C for 5 min and gradually cooled down to 25°C at the rate of 0.2°C min^{-1} to facilitate quadruplex formation for the biophysical studies. Twist control 2, a synthetic SARS-CoV-2 RNA template obtained from Twist Bioscience was used as the template RNA for the reverse transcription inhibition assay. MTT was procured from Sigma (M2128).

4.2 Biological resources

Cell lines- Vero CCL-81, Vero E6.

Viruses- Isolate of B.6 strain of SARS-CoV-2, Isolate USA-WA1/2020 of SARS-CoV-2.

Animals- 6–8 weeks old male golden Syrian hamsters were procured from CSIR-CDRI, Lucknow, India.

4.3 Estimation of genome wide mutation frequencies and conservation analysis of pG4s

Genome wide mutation counts of globally circulating SARS CoV-2 genomes were retrieved from China National Center for Bioinformation (CNCB) (National Genomics Data Center, n.d.). This site provides the comprehensive details of over 29000 variation sites observed from about 5.4 million SARS-CoV-2 genomes worldwide. The frequency of mutations at each nucleotide site were systematically estimated using Microsoft excel functions. The circos plot in Figure 1A was prepared using ggplot2 package in R. The line histogram in Figure 1B was prepared using GraphPad Prism. In addition, the mutation frequency of the pG4 motifs was analyzed by estimating the average mutation frequency of each of the Guanines involved in G4 tetrad formation.

4.4 Circular dichroism (CD) spectroscopy

CD spectra experiments were carried out on JASCO J-815 spectropolarimeter equipped with a temperature-controlled cell holder and a cuvette with a path length of 1 cm. The oligos were used after going through the quadruplex formation procedure mentioned in the Materials section. Differential absorption spectra were recorded in the 200–300 nm range at room temperature. The represented spectrum is an automated average of three consecutive scans for each sample. CD titrations were carried out by the stepwise addition of CPZ or PCZ (up to 5 μM) to a cell containing 5 μM RNA oligo.

4.5 Fluorescence assays

The assays were carried out on Horiba Scientific Fluoromax-4 spectrofluorometer at 25°C. For NMM treated samples, emission spectra were measured by using an excitation wavelength of 399 nm. The concentration of NMM and the RNA oligos was fixed at 1 μM. The oligos were used after going through the quadruplex formation procedure mentioned in the Materials section. For the displacement assay, the concentration of NMM and the RNA oligos was fixed at 1 μM while CPZ and PCZ were added in increasing molar equivalents.

4.6 Isothermal titration calorimetry (ITC)

ITC measurements were carried out in a PEAQ- ITC titration calorimeter (Malvern Panalytical). Before loading, the solutions were thoroughly degassed. The oligos were used after going through the quadruplex formation procedure mentioned in the Materials section. The RNA oligo (15 μM) was kept in the sample cell, and 80 μl of CPZ/PCZ (1,000 μM) dissolved in the same buffer (10 mM sodium cacodylate with 100 mM KCl) was filled in the syringe. Ligand solution was added sequentially in 3 μl aliquots (for a total of 13 injections, 6 s duration each) at 180 s intervals at 25°C. For CPZ, the integrated heat data were fit with one binding site model using the Microcal PEAQ ITC analysis software. For PCZ, due to the non-sigmoidal shape of the thermogram and the obvious presence of at least two independent binding processes, the thermogram obtained in ITC experiments was fit with two independent sites model in Microcal PEAQ ITC analysis software. Finally, the data was plotted using Origin pro 8.5 software.

4.7 Reverse transcription inhibition assay

Inspired from reverse transcriptase stalling used to identify RNA G4s, a reverse transcription assay from synthetic SARS-CoV-2 genomic RNA was done in presence of CPZ/PCZ (Kwok et al., 2016). Twist control 2, a synthetic SARS-CoV2 RNA template obtained from Twist Bioscience was used as the template RNA for this assay. The synthetic RNA template was reverse transcribed using Superscript II reverse transcriptase obtained from Invitrogen, in presence of 50 μM of KCl. Reverse transcription was done using reverse primers such that ORF1 pG4-1 or a non G4 forming control region (NC_045512v2: 28,654-28,758, UCSC genome browser) gets reverse transcribed (primer sequences below). Different concentrations of CPZ and PCZ were added in the reverse transcription reactions and compared against no drug treatment. The efficiency of the reverse transcription reactions was measured by quantifying the generated cDNA by qPCR using primers overlapping the ORF1 pG4 or the non G4 forming control region (primer sequences below). The same experiment was also done using RNA isolated from nasopharyngeal swabs of COVID-19 infected individuals following approvals by the Institutional Human Ethics Committee (IGIB) while abiding by the Declaration of Helsinki principles. For Figure 4A, 5×10^4 copies of the synthetic SARS-CoV-2 RNA template was used in each reverse transcription reaction. For Figure 4B, 2 μl of RNA samples obtained from patients with high viral load (cT values between 15 and 20 obtained in diagnostic qRT-PCR for detection of COVID-19 infection using STANDARD M nCoV Real-Time Detection Kit manufactured by SD BIOSENSOR) was used in each reverse transcription reaction.

4.8 Cell culture

All inhibition experiments were carried out on African green monkey kidney cells (Vero CCL-81). The cells were cultured in

Target	Forward	Reverse
ORF1 pG4-1	CACATGCAGAAGAAACACGC	AGTGTGTTGATAAGTGACGCT
Non G4 Control	AGACGGCATCATATGGGTTG	GGAAGTTGTAGCACGATTGC

Dulbecco's modified Eagle's medium (DMEM, Gibco) supplemented with 10% heat inactivated Fetal Bovine Serum (Gibco) and $1 \times$ Pen Strep (Gibco).

4.9 Virus generation

An isolate of B.6 strain of SARS-CoV-2 was used in this study. The isolation and characterization were described previously (Gupta et al., 2021). In brief, viral transport media was first filtered through a 0.22 μm filter and was used as inoculum on Vero cells in a 96-well format. Upon the appearance of visible cytopathic effects (CPE), the viral culture supernatant was used to infect fresh cells to amplify the viral titer. The process was repeated until the supernatant displayed infectious titer in the range of 10^{-7}ml^{-1}.

4.10 Cell infection and pharmacological (G4 ligands) treatment

Vero cells were seeded in a 12-well format. At 90% confluency, cells were either mock-infected or infected with 1 MOI of SARS-CoV-2 in serum-free medium for 3 h in the presence of CPZ or PCZ. Subsequently, the viral inoculum was replaced with growth medium containing 10% FBS medium and CPZ/PCZ, or the vehicle controls (same volume either water or DMSO). After 24 h post infection (hpi), the media was replaced with fresh growth medium with the respective compounds, and cultured for another 24 h. At 48 hpi, the cell culture supernatants were collected to measure infectious particle count through PFU and extracellular viral RNA using quantitative real time PCR.

4.11 Virus titration (PFU)

The virus was titrated using PFU (Plaque-Forming Unit) assay in Vero cells following protocol mentioned in (Gupta et al., 2021). Briefly Vero cells were seeded in 12-well plate at 90% confluency. The viral culture supernatant obtained after CPZ/PCZ treatment (mentioned above) was log-diluted from 10-1 to 10-7 in serum-free media and was added to a 100% confluent monolayer of Vero cells. Three hours post-infection the infection inoculum was replaced with agar media (one part of 2% low melting point agarose (LMA) mixed with one part of $2 \times$ DMEM with 5% FBS and 1% Pen-Strep). 6–7 days post-infection, cells were fixed with 4% formaldehyde in $1 \times$ PBS and stained with 0.1% crystal violet. The dilution which had 5–20 plaques was used for calculating PFU/ml. Each dilution was assayed in duplicate and the values from the duplicate wells were averaged before calculating the respective PFU.

4.12 RNA isolation and real-time qPCR

RNA from cell culture supernatant after CPZ/PCZ treatment (mentioned above) was isolated using viral RNA isolation kit (MACHEREY-NAGEL GmbH & Co. KG). Real-time quantitative RT-PCR was performed in Roche LightCycler 480 using commercial kits. LabGun™ COVID-19 RT-PCR Kit was used to measure the RNA levels of SARS-CoV-2 RdRp and E genes while Fosun COVID-19 RT-PCR Kit was used to measure the RNA levels of SARS-CoV-2 ORF1ab and N genes following manufacturers' protocol. Fold changes between samples were calculated by $\Delta\Delta$ Cp method using the internal control (IC) for normalization.

4.13 Cytotoxicity assay

The cytotoxicity of the drugs used in the study was determined using MTT ((3-[4,5-dimethylthylthiazol-2-yl]-2,5-diphenyl) assay. Following the above-mentioned infection and CPZ/PCZ treatment, MTT was added to the cells at 24 hpi at final concentration of 0.5 mg/mL in fresh media, following 6 h of incubation at 37°C, media was aspirated and formazan crystals were dissolved in 100 μl of 100% DMSO, plates were incubated at RT for 20 min with constant shaking and readings at 570 nm were taken. A cell-free medium control was included to account for background due to phenol red in the medium.

4.14 Animals

6–8 weeks old male golden Syrian hamsters were procured from CDRI and transported to small animal facility (SAF), THSTI and quarantined for 7 days. During the pre-treatment regime the animals were housed at small animal facility (SAF) and then were transferred to the Animal biosafety level-3 (ABSL-3) institutional facility for SARS-CoV-2 challenge study. The animals were maintained under 12 h light and dark cycle and fed standard pellet diet and water *ad libitum*. All the experimental protocols involving dosing and animal challenge were approved by institutional IAEC, IBS and RCGM.

4.15 Virus generation for animal experiments

SARS-Related Coronavirus 2, Isolate USA-WA1/2020 virus was grown and titrated in Vero E6 cell line cultured in Dulbecco's Modified Eagle Medium (DMEM) complete media containing 4.5 g/L D-glucose, 100,000 U/L Penicillin-Streptomycin, 100 mg/L sodium pyruvate, 25 mM HEPES and 2% FBS. The stocks of virus were plaque purified at THSTI IDRF facility inside ABSL3 following institutional biosafety guidelines.

Gene	Forward	Reverse
HGPRT	GATAGATCCACTCCCATAACTG	TACCTTCAACAATCAAGACATTC
SARS-Cov-2 N gene	GACCCCAAAATCAGCGAAAT	TCTGGTTACTGCCAGTTGAATCTG

4.16 SARS-CoV2 infection in golden syrian hamster and dosing

Golden Syrian hamsters were randomly allotted to different drug groups (n = 4), challenge control (n = 2), remdesivir control (n = 2) and unchallenged control (n = 2) were housed in separate cages. The remdesivir group received a subcutaneous injection of remdesivir at 15 mg/kg body weight 1 day before and 1 day post infection (Rizvi et al., 2022b). The pre-treatment group viz pCPZ & pPCZ started receiving 8 mg/kg and 5 mg/kg (respectively) of the drug through intraperitoneal administration each day starting from 3 days prior to the challenge and continued till end point (day 4 post infection). The therapeutic groups viz tCPZ and tPCZ received the drug 8 mg/kg and 5 mg/kg (respectively) through intra-peritoneal injection from the day of challenge for each day till the end point (Diaconu et al., 2010; Simanjuntak et al., 2015). All the animals, except unchallenged control, were challenged with 10^5 PFU of SARS-CoV2 administered intranasally (50ul/nare) using a catheter while under anesthesia by using ketamine (150 mg/kg) and xylazine (10 mg/kg) intraperitoneal injection inside ABSL3 facility (Chan et al., 2020; Sia et al., 2020; Rizvi et al., 2021). Unchallenged control group received mock PBS intranasally. All the experimental protocols involving the handling of virus culture and animal infection were approved by RCGM, institutional biosafety and IAEC animal ethics committee.

4.17 Gross clinical parameters of SARS-CoV2 infection

All infected animals were euthanized on 4 days post infection at ABSL3. Changes in body weight, activity of the animals were observed on each day post challenge. Post sacrifice, lungs and spleen of the animals were excised and imaged for gross morphological changes (Rizvi et al., 2021, 2022b). Right lower lobe of the lung was fixed in 10% neutral formalin solution and used for histological analysis. The complete left lobe of the lung was homogenized in 2 ml Trizol solution for viral load estimation. Spleen was homogenized in 2 ml of Trizol solution. The tissue samples in trizol were stored immediately at −80°C till further use.

4.18 Lung viral load qPCR

RNA was isolated from the lung samples using Trizol-choloroform method. Thereafter, RNA was quantitated by NanoDrop and 1 µg of total RNA was then reverse-transcribed to cDNA using the iScript cDNA synthesis kit (Biorad; #1708891) (Roche). Diluted cDNA (1:5) were used for qPCR by using KAPA

SYBR® FAST qPCR Master Mix (5X) universal Kit (KK4600) on Fast 7500 Dx real-time PCR system (Applied Biosystems) and the results were analyzed with SDS2.1 software. We assessed the relative expression of SARS-CoV-2 N gene in the RNA isolated from the lung samples for estimation of the lung viral load. The relative expression of each gene was expressed as fold change and was calculated by subtracting the cycling threshold (Ct) value of hypoxantine-guanine phosphoribosyltransferase (HGPRT-endogenous control gene) from the Ct value of target gene (ΔCT). Following primers were used (Rizvi et al., 2021).

4.19 Lung histology

Fixed lungs were processed and paraffin wax embedded blocks were transverse sectioned and stained with hematoxylin and eosin. The H & E-stained lung sections was then quantitatively examined under the microscope for pneumonitis, alveolar epithelial cell injury, inflammation, and lung injury on the scale of 0-5 by expert histologist. Images of the HE stained lungs sections were acquired at ×40 magnification.

4.20 Statistical analysis of data

p-values for the animal studies were calculated using ordinary one-way ANOVA for statistical significance. For all other experiments done in triplicates p-values were calculated using Student's t-test for statistical significance (*$p < 0.05$, **$p < 0.01$, ***$p < 0.005$).

Data availability statement

The original contributions presented in the study are included in the article/Supplementary Material, further inquiries can be directed to the corresponding author.

Ethics statement

The studies involving human participants were reviewed and approved by Institutional Human Ethics Committee (IGIB). The patients/participants provided their written informed consent to participate in this study. The animal study was reviewed and approved by IAEC, IBS and RCGM at THSTI.

Author contributions

SC: Conceptualization, methodology, resources, writing—original draft, review and editing, supervision, project

Funding

Acknowledgments

Conflict of interest

The authors declare that the research was conducted in the absence of any commercial or financial relationships that could be construed as a potential conflict of interest.

Publisher's note

All claims expressed in this article are solely those of the authors and do not necessarily represent those of their affiliated organizations, or those of the publisher, the editors and the reviewers. Any product that may be evaluated in this article, or claim that may be made by its manufacturer, is not guaranteed or endorsed by the publisher.

Supplementary material

The Supplementary Material for this article can be found online at: https://www.frontiersin.org/articles/10.3389/fmolb.2023.1133123/full#supplementary-material

References

Abiri, A., Lavigne, M., Rezaei, M., Nikzad, S., Zare, P., Mergny, J. L., et al. (2021). Unlocking G-quadruplexes as antiviral targets. *Pharmacol. Rev.* 73, 897–923. doi:10.1124/PHARMREV.120.000230

Arora, A., Dutkiewicz, M., Scaria, V., Hariharan, M., Maiti, S., and Kurreck, J. (2008). Inhibition of translation in living eukaryotic cells by an RNA G-quadruplex motif. *RNA* 14, 1290–1296. doi:10.1261/RNA.1001708

Baral, A., Kumar, P., Halder, R., Mani, P., Yadav, V. K., Singh, A., et al. (2012). Quadruplex-single nucleotide polymorphisms (Quad-SNP) influence gene expression difference among individuals. *Nucleic Acids Res.* 40, 3800–3811. doi:10.1093/nar/gkr1258

Beaudoin, J. D., Jodoin, R., and Perreault, J. P. (2014). New scoring system to identify RNA G-quadruplex folding. *Nucleic Acids Res.* 42, 1209–1223. doi:10.1093/NAR/GKT904

Bedrat, A., Lacroix, L., and Mergny, J. L. (2016). Re-evaluation of G-quadruplex propensity with G4Hunter. *Nucleic Acids Res.* 44, 1746–1759. doi:10.1093/NAR/GKW006

Beigel, J. H., Tomashek, K. M., Dodd, L. E., Mehta, A. K., Zingman, B. S., Kalil, A. C., et al. (2020). Remdesivir for the treatment of covid-19 — final report. *N. Engl. J. Med.* 383, 1813–1826. doi:10.1056/NEJMOA2007764

Bezzi, G., Piga, E. J., Binolfi, A., and Armas, P. (2021). Cnbp binds and unfolds *in vitro* g-quadruplexes formed in the sars-cov-2 positive and negative genome strands. *Int. J. Mol. Sci.* 22, 2614–2622. doi:10.3390/ijms22052614

Boudewijns, R., Thibaut, H. J., Kaptein, S. J. F., Li, R., Vergote, V., Seldeslachts, L., et al. (2020). STAT2 signaling restricts viral dissemination but drives severe pneumonia in SARS-CoV-2 infected hamsters. *Nat. Commun.* 11, 5838–5910. doi:10.1038/s41467-020-19684-y

Burkard, C., Verheije, M. H., Wicht, O., van Kasteren, S. I., van Kuppeveld, F. J., Haagmans, B. L., et al. (2014). Coronavirus cell entry occurs through the endo-/lysosomal pathway in a proteolysis-dependent manner. *PLOS Pathog.* 10, e1004502. doi:10.1371/JOURNAL.PPAT.1004502

Butovskaya, E., Soldà, P., Scalabrin, M., Nadai, M., and Richter, S. N. (2019). HIV-1 nucleocapsid protein unfolds stable RNA G-quadruplexes in the viral genome and is inhibited by G-quadruplex ligands. *ACS Infect. Dis.* 5, 2127–2135. doi:10.1021/acsinfecdis.9b00272

Castillo-Gonzalez, D., Perez-Machado, G., Guedin, A., Mergny, J.-L., and Cabrera-Perez, M.-A. (2013). FDA-Approved drugs selected using virtual screening bind specifically to G-quadruplex DNA. *Curr. Pharm. Des.* 19, 2164–2173. doi:10.2174/1381612811319120004

Chamoun-Emanuelli, A. M., Pecheur, E. I., Simeon, R. L., Huang, D., Cremer, P. S., and Chena, Z. (2013). Phenothiazines inhibit hepatitis C virus entry, likely by increasing the fluidity of cholesterol-rich membranes. *Antimicrob. Agents Chemother.* 57, 2571–2581. doi:10.1128/AAC.02593-12

Chan, J. F. W., Zhang, A. J., Yuan, S., Poon, V. K. M., Chan, C. C. S., Lee, A. C. Y., et al. (2020). Simulation of the clinical and pathological manifestations of coronavirus disease 2019 (COVID-19) in a golden Syrian hamster model: Implications for disease pathogenesis and transmissibility. *Pathog. Transm.* 71, 2428–2446. doi:10.1093/CID/CIAA325

Chen, X., Cao, R., and Zhong, W. (2019). Host calcium channels and pumps in viral infections. *Cells* 9, 94. doi:10.3390/CELLS9010094

Choi, S. Y., Kim, Y. H., Lee, Y. K., and Kim, K. T. (2001). Chlorpromazine inhibits store-operated calcium entry and subsequent noradrenaline secretion in PC12 cells. *Br. J. Pharmacol.* 132, 411–418. doi:10.1038/SJ.BJP.0703840

Cong, Y., Hart, B. J., Gross, R., Zhou, H., Frieman, M., Bollinger, L., et al. (2018). MERS-CoV pathogenesis and antiviral efficacy of licensed drugs in human monocyte-derived antigen-presenting cells. *PLoS One* 13, e0194868. doi:10.1371/JOURNAL.PONE.0194868

David, A. P., Pipier, A., Pascutti, F., Binolfi, A., Weiner, A. M. J., Challier, E., et al. (2019). CNBP controls transcription by unfolding DNA G-quadruplex structures. *Nucleic Acids Res.* 47, 7901–7913. doi:10.1093/NAR/GKZ527

del Villar-Guerra, R., Trent, J. O., and Chaires, J. B. (2018). G-quadruplex secondary structure obtained from circular dichroism spectroscopy. *Angew. Chem.* 130, 7289–7293. doi:10.1002/ANGE.201709184

Dhapola, P., and Chowdhury, S. (2016). QuadBase2: Web server for multiplexed guanine quadruplex mining and visualization. *Nucleic Acids Res.* 44, W277–W283. doi:10.1093/nar/gkw425

Diaconu, I., Cerullo, V., Escutenaire, S., Kanerva, A., Bauerschmitz, G. J., Hernandez-Alcoceba, R., et al. (2010). Human adenovirus replication in immunocompetent Syrian hamsters can be attenuated with chlorpromazine or cidofovir. *J. Gene Med.* 12, 435–445. doi:10.1002/JGM.1453

Dransfield, G. A. (1958). A clinical trial comparing prochlorperazine ("Stemetil") with chlorpromazine ("Largactil") in the treatment of chronic psychotic patients. *J. Ment. Sci.* 104, 1183–1189. doi:10.1192/BJP.104.437.1183

Fred, S. M., Kuivanen, S., Ugurlu, H., Casarotto, P. C., Levanov, L., Saksela, K., et al. (2022). Antidepressant and antipsychotic drugs reduce viral infection by SARS-CoV-2 and fluoxetine shows antiviral activity against the novel variants *in vitro. Front. Pharmacol.* 12, 3854. doi:10.3389/fphar.2021.755600

Garant, J. M., Perreault, J. P., and Scott, M. S. (2017). Motif independent identification of potential RNA G-quadruplexes by G4RNA screener. *Bioinformatics* 33, 3532–3537. doi:10.1093/BIOINFORMATICS/BTX498

Garant, J. M., Perreault, J. P., and Scott, M. S. (2018). G4RNA screener web server: User focused interface for RNA G-quadruplex prediction. *Biochimie* 151, 115–118. doi:10.1016/J.BIOCHI.2018.06.002

Gupta, D., Parthasarathy, H., Sah, V., Tandel, D., Vedagiri, D., Reddy, S., et al. (2021). Inactivation of SARS-CoV-2 by β-propiolactone causes aggregation of viral particles and loss of antigenic potential. *Virus Res.* 305, 198555. doi:10.1016/J.VIRUSRES.2021.198555

Hon, J., Martínek, T., Zendulka, J., and Lexa, M. (2017). pqsfinder: an exhaustive and imperfection-tolerant search tool for potential quadruplex-forming sequences in R. *Bioinformatics* 33, 3373–3379. doi:10.1093/bioinformatics/btx413

Janik, E., Niemcewicz, M., Podogrocki, M., Saluk-Bijak, J., and Bijak, M. (2021). Existing drugs considered as promising in COVID-19 therapy. *Int. J. Mol. Sci.* 22, 5434. doi:10.3390/IJMS22115434

Jayaseelan, V. P., and Paramasivam, A. (2020). Repurposing calcium channel blockers as antiviral drugs. *J. Cell Commun. Signal.* 14, 467–468. doi:10.1007/S12079-020-00579-Y

Ji, D., Juhas, M., Tsang, C. M., Kwok, C. K., Li, Y., and Zhang, Y. (2021). Discovery of G-quadruplex-forming sequences in SARS-CoV-2. *Brief. Bioinform* 22, 1150–1160. doi:10.1093/bib/bbaa114

Kelleni, M. T. (2021). Early use of non-steroidal anti-inflammatory drugs in COVID-19 might reverse pathogenesis, prevent complications and improve clinical outcomes. *Biomed. Pharmacother.* 133, 110982. doi:10.1016/J.BIOPHA.2020.110982

Kharel, P., Becker, G., Tsvetkov, V., and Ivanov, P. (2020). Properties and biological impact of RNA G-quadruplexes: From order to turmoil and back. *Nucleic Acids Res.* 48, 12534–12555. doi:10.1093/NAR/GKAA1126

Kikin, O., D'Antonio, L., and Bagga, P. S. (2006). QGRS mapper: A web-based server for predicting G-quadruplexes in nucleotide sequences. *Nucleic Acids Res.* 34, W676–W682. doi:10.1093/nar/gkl253

Kreig, A., Calvert, J., Sanoica, J., Cullum, E., Tipanna, R., and Myong, S. (2015). G-quadruplex formation in double strand DNA probed by NMM and CV fluorescence. *Nucleic Acids Res.* 43, 7961–7970. doi:10.1093/nar/gkv749

Kreye, J., Reincke, S. M., Kornau, H. C., Sánchez-Sendin, E., Corman, V. M., Liu, H., et al. (2020). A therapeutic non-self-reactive SARS-CoV-2 antibody protects from lung pathology in a COVID-19 hamster model. *Cell* 183, 1058–1069. doi:10.1016/J.CELL.2020.09.049

Kwok, C. K., Marsico, G., Sahakyan, A., Chambers, V. S., and Balasubramanian, S. (2016). RG4-seq reveals widespread formation of G-quadruplex structures in the human transcriptome. *Nat. Methods* 13, 841–844. doi:10.1038/nmeth.3965

Lai, A. L., Millet, J. K., Daniel, S., Freed, J. H., and Whittaker, G. R. (2017). The SARS-CoV fusion peptide forms an extended bipartite fusion platform that perturbs membrane order in a calcium-dependent manner. *J. Mol. Biol.* 429, 3875–3892. doi:10.1016/J.JMB.2017.10.017

Lavigne, M., Helynck, O., Rigolet, P., Boudria-Souilah, R., Nowakowski, M., Baron, B., et al. (2021). SARS-CoV-2 Nsp3 unique domain SUD interacts with guanine quadruplexes and G4-ligands inhibit this interaction. *Nucleic Acids Res.* 49, 7695–7712. doi:10.1093/nar/gkab571

Lee, A. C. Y., Zhang, A. J., Chan, J. F. W., Li, C., Fan, Z., Liu, F., et al. (2020). Oral SARS-CoV-2 inoculation establishes subclinical respiratory infection with virus shedding in golden Syrian hamsters. *Cell Rep. Med.* 1, 100121. doi:10.1016/J.XCRM.2020.100121

Liu, G., Du, W., Sang, X., Tong, Q., Wang, Y., Chen, G., et al. (2022). RNA G-quadruplex in TMPRSS2 reduces SARS-CoV-2 infection. *Nat. Commun.* 131, 1444–1513. doi:10.1038/s41467-022-29135-5

Lv, L., Cui, H., Chen, Z., Zhou, Y., and Zhang, L. (2022). G-quadruplex ligands inhibit chikungunya virus replication. *J. Med. Virol.* 94, 2519–2527. doi:10.1002/JMV.27622

Lyu, K., Chow, E. Y. C., Mou, X., Chan, T. F., and Kwok, C. K. (2021). RNA G-quadruplexes (rG4s): Genomics and biological functions. *Nucleic Acids Res.* 49, 5426–5450. doi:10.1093/NAR/GKAB187

Majee, P., Pattnaik, A., Sahoo, B. R., Shankar, U., Pattnaik, A. K., Kumar, A., et al. (2021). Inhibition of Zika virus replication by G-quadruplex-binding ligands. *Mol. Ther. Nucleic Acids* 23, 691–701. doi:10.1016/J.OMTN.2020.12.030

Mergny, J. L., and Helene, C. (1998). G-Quadruplex DNA: A target for drug design. *Nat. Med.* 4, 1366–1367. doi:10.1038/3949

Mukherjee, A. K., Sharma, S., and Chowdhury, S. (2019). Non-duplex G-quadruplex structures emerge as mediators of epigenetic modifications. *Trends Genet.* 35, 129–144. doi:10.1016/j.tig.2018.11.001

Murat, P., Zhong, J., Lekieffre, L., Cowieson, N. P., Clancy, J. L., Preiss, T., et al. (2014). G-quadruplexes regulate Epstein-Barr virus–encoded nuclear antigen 1 mRNA translation. *Nat. Chem. Biol.* 105 (10), 358–364. doi:10.1038/nchembio.1479

Nemani, K., Williams, S. Z., Olfson, M., Leckman-Westin, E., Finnerty, M., Kammer, J., et al. (2022). Association between the use of psychotropic medications and the risk of COVID-19 infection among long-term inpatients with serious mental illness in a New York state–wide psychiatric hospital system. *JAMA Netw. Open* 5, e2210743. doi:10.1001/JAMANETWORKOPEN.2022.10743

Panera, N., Tozzi, A. E., and Alisi, A. (2020). The G-quadruplex/helicase world as a potential antiviral approach against COVID-19. *Drugs* 80, 941–946. doi:10.1007/s40265-020-01321-z

Plaze, M., Attali, D., Prot, M., Petit, A. C., Blatzer, M., Vinckier, F., et al. (2021). Inhibition of the replication of SARS-CoV-2 in human cells by the FDA-approved drug chlorpromazine. *Int. J. Antimicrob. Agents* 57, 106274. doi:10.1016/J.IJANTIMICAG.2020.106274

Pruijssers, A. J., George, A. S., Schäfer, A., Leist, S. R., Gralinksi, L. E., Dinnon, K. H., et al. (2020). Remdesivir inhibits SARS-CoV-2 in human lung cells and chimeric SARS-CoV expressing the SARS-CoV-2 RNA polymerase in mice. *Cell Rep.* 32, 107940. doi:10.1016/J.CELREP.2020.107940

Rawal, P., Kummarasetti, V. B. R., Ravindran, J., Kumar, N., Halder, K., Sharma, R., et al. (2006). Genome-wide prediction of G4 DNA as regulatory motifs: Role in *Escherichia coli* global regulation. *Genome Res.* 16, 644–655. doi:10.1101/gr.4508806

Rizvi, Z. A., Tripathy, M. R., Sharma, N., Goswami, S., Srikanth, N., Sastry, J. L. N., et al. (2021). Effect of prophylactic use of intranasal oil formulations in the hamster model of COVID-19. *Front. Pharmacol.* 12, 746729–746811. doi:10.3389/fphar.2021.746729

Rizvi, Z. A., Babele, P., Sadhu, S., Madan, U., Tripathy, M. R., Goswami, S., et al. (2022a). Prophylactic treatment of Glycyrrhiza glabra mitigates COVID-19 pathology through inhibition of pro-inflammatory cytokines in the hamster model and NETosis. *Front. Immunol.* 13, 5613. doi:10.3389/fimmu.2022.945583

Rizvi, Z. A., Dalal, R., Sadhu, S., Binayke, A., Dandotiya, J., Kumar, Y., et al. (2022b). Golden Syrian hamster as a model to study cardiovascular complications associated with SARS-CoV-2 infection. *Elife* 11, e73522. doi:10.7554/eLife.73522

Rosenke, K., Jarvis, M. A., Feldmann, F., Schwarz, B., Okumura, A., Lovaglio, J., et al. (2020). Hydroxychloroquine prophylaxis and treatment is ineffective in macaque and hamster SARS-CoV-2 disease models. *JCI Insight* 5, e143174. doi:10.1172/JCI.INSIGHT.143174

Ruggiero, E., and Richter, S. N. (2018). G-Quadruplexes and G-quadruplex ligands: Targets and tools in antiviral therapy. *Nucleic Acids Res.* 46, 3270–3283. doi:10.1093/nar/gky187

Ruggiero, E., and Richter, S. N. (2020). Viral G-quadruplexes: New frontiers in virus pathogenesis and antiviral therapy. *Annu. Rep. Med. Chem.* 54, 101–131. doi:10.1016/BS.ARMC.2020.04.001

Ruggiero, E., Zanin, I., Terreri, M., and Richter, S. N. (2021). G-quadruplex targeting in the fight against viruses: An update. *Int. J. Mol. Sci.* 22, 10984. doi:10.3390/ijms222010984

Schmidt, N., Lareau, C. A., Keshishian, H., Ganskih, S., Schneider, C., Hennig, T., et al. (2021). The SARS-CoV-2 RNA–protein interactome in infected human cells. *Nat. Microbiol.* 6, 339–353. doi:10.1038/s41564-020-00846-z

Sengupta, A., Roy, S. S., and Chowdhury, S. (2020). Non-duplex G-quadruplex DNA structure: A developing story from predicted sequences to DNA structure-dependent epigenetics and beyond. *Acc. Chem. Res.* 54, 46–56. doi:10.1021/ACS.ACCOUNTS.0C00431

Sia, S. F., Yan, L. M., Chin, A. W. H., Fung, K., Choy, K. T., Wong, A. Y. L., et al. (2020). Pathogenesis and transmission of SARS-CoV-2 in golden hamsters. *Nature* 583, 834–838. Available at: https://www.nature.com/articles/s41586-020-2342-5. doi:10.1038/s41586-020-2342-5

Simanjuntak, Y., Liang, J. J., Lee, Y. L., and Lin, Y. L. (2015). Repurposing of prochlorperazine for use against dengue virus infection. *J. Infect. Dis.* 211, 394–404. doi:10.1093/INFDIS/JIU377

Stip, E., Rizvi, T. A., Mustafa, F., Javaid, S., Aburuz, S., Ahmed, N. N., et al. (2020). The large action of chlorpromazine: Translational and transdisciplinary considerations in the face of COVID-19. *Front. Pharmacol.* 11, 1826. doi:10.3389/fphar.2020.577678

Straus, M. R., Tang, T., Lai, A. L., Flegel, A., Bidon, M., Freed, J. H., et al. (2020). Ca 2+ ions promote fusion of Middle East respiratory syndrome coronavirus with host cells and increase infectivity. *J. Virol.* 94, 426–446. doi:10.1128/JVI.00426-20

Thakur, R. K., Kumar, P., Halder, K., Verma, A., Kar, A., Parent, J. L., et al. (2009). Metastases suppressor NM23-H2 interaction with G-quadruplex DNA within c-MYC promoter nuclease hypersensitive element induces c-MYC expression. *Nucleic Acids Res.* 37, 172–183. doi:10.1093/nar/gkn919

Tostanoski, L. H., Wegmann, F., Martinot, A. J., Loos, C., McMahan, K., Mercado, N. B., et al. (2020). Ad26 vaccine protects against SARS-CoV-2 severe clinical disease in hamsters. *Nat. Med.* 26, 1694–1700. doi:10.1038/s41591-020-1070-6

Varshney, D., Spiegel, J., Zyner, K., Tannahill, D., and Balasubramanian, S. (2020). The regulation and functions of DNA and RNA G-quadruplexes. *Nat. Rev. Mol. Cell Biol.* 21, 459–474. doi:10.1038/s41580-020-0236-x

Verma, A., Halder, K., Halder, R., Yadav, V. K., Rawal, P., Thakur, R. K., et al. (2008). Genome-wide computational and expression analyses reveal G-quadruplex DNA motifs as conserved cis-regulatory elements in human and related species. *J. Med. Chem.* 51, 5641–5649. doi:10.1021/jm800448a

Yadav, V. K., Abraham, J. K., Mani, P., Kulshrestha, R., and Chowdhury, S. (2008). QuadBase: Genome-wide database of G4 DNA - occurrence and conservation in human, chimpanzee, mouse and rat promoters and 146 microbes. *Nucleic Acids Res.* 36, 381–385. doi:10.1093/nar/gkm781

Zhang, R., Xiao, K., Gu, Y., Liu, H., and Sun, X. (2020). Whole genome identification of potential G-quadruplexes and analysis of the G-quadruplex binding domain for SARS-CoV-2. *Front. Genet.* 11, 1430. doi:10.3389/fgene.2020.587829

Zhao, C., Qin, G., Niu, J., Wang, Z., Wang, C., Ren, J., et al. (2021). Targeting RNA G-quadruplex in SARS-CoV-2: A promising therapeutic target for COVID-19? *Angew. Chem. - Int. Ed.* 60, 432–438. doi:10.1002/anie.202011419